# Electro- and photon-induced cooling in BNT-BT-SBET relaxors with *in situ* optical temperature sensing


**Lejian Wang,[1] Jingji Zhang,[1,*] Jiangying Wang,[1,*] Yaxuan Yao,[2] Lingling Ren,[2] Xue Chen,[3] Martin Birkett,[3] Laurent Dala,[3] Ben Xu,[3,*]**

[1]*College of Materials and Chemistry, China Jiliang University, Hangzhou 310018, P. R. China*
[2]*Center for advanced metrology science, National Institute of Metrology, Beijing 100013, P. R. China*
[3]*Department of Mechanical and Construction Engineering, Faculty of Engineering and Environment, Northumbria University, Newcastle upon Tyne, NE1 8ST, UK*
**Corresponding author: apzhjj@163.com; wjyliu@163.com; renll@nim.ac.cn; ben.xu@northumbria.ac.uk.*



Received XX Month XXXX; revised XX Month, XXXX; accepted XX Month XXXX; posted XX Month XXXX (Doc. ID XXXXX); published XX Month XXXX



**A novel lead-free luminescent ferroelectric (FE) ceramic, $Bi_{0.5}Na_{0.5}TiO_3$-0.06$BaTiO_3$-0.055$Sr_{0.7}Bi_{0.18}Er_{0.02}\square_{0.1}TiO_3$, is developed with an adiabatic temperature change ($\Delta T$) of 0.7 K under an electric-field ($E$) of 60 kV/cm at room temperature (RT), an anti-stokes fluorescence (FL) cooling and a maximum optical $T$ sensitivity of 0.0055 $K^{-1}$ at 522 K. Interestingly, the electrocaloric (EC) response reaches a saturation at permittivity-shoulder $T$ of 100 °C, meanwhile the maximized emission intensity of $^2H_{11/2}\rightarrow{}^4I_{15/2}$ occurs. $T$- and $E$-tunable enhancement of $^2H_{11/2}\rightarrow{}^4I_{15/2}$ emission intensity is due to the population inversion from the $^4S_{3/2}$ to $^2H_{11/2}$ states caused by an incoherent regime consisting of FE phase and polar nanoregions (PNRs) in a relaxor (R) matrix. © 2019 Optical Society of America**



http://dx.doi.org/10.1364/OL.99.099999


Major progress has recently been made in solid-state refrigeration in the substitution of bulky and noisy vapor-compression system that currently dominates the market. Current research is mainly focused on monocaloric effect[1], such as thermoelectric[2], magnetocaloric[3], barocaloric[4], elastocaloric[5], EC[6], and anti-stokes FL[7]. Although an $\Delta T$ above 40 K can be obtained for some monocaloric effects[4, 8], it requires a precision control of target-$T$ rather than very low target-$T$ for enormous portable devices and wearable electronics in modern society. Usually, a complicated $T$ controlling system needs to be equipped, which increases product cost and is difficult to scale down.

Rare-earth doped FE, a stimuli-responsive material, has attracted significant interests owing to its ability to respond to multiple stimuli (such as $E$, magnetic, mechanical stress/strain, photons)[9-11] and its high designability on functions[12]. Applying an $E$ to or removing it from FE matrix induces the variation of polarization state, leading to $\Delta T$, which is known as EC effect[13-16]. The application of long wavelength light to rare-earth doped matrix induces shorter wavelength FL photons, releasing heat from the matrix, which is FL cooling[17, 18]. Due to the unique energy level configuration of $Er^{3+}$, FL cooling can be obtained in $Er^{3+}$-doped materials by three anti-stokes emitting routes[19, 20]: (i) the transition between the higher stark splitting levels of excited state $^4I_{13/2}$ and ground state $^4I_{15/2}$, (ii) the upconversion (UC) process by selectively pumping at the low energy side of $^4I_{9/2}$ manifold, and (iii) the transition of $^4S_{3/2}\rightarrow{}^2H_{11/2}$. Among these FL cooling processes, the third process has larger cooling efficiency since the wavelength difference between $^4S_{3/2}$ and $^2H_{11/2}$ levels is much larger than those of the former two routes[19]. In addition, by applying FL intensity ratio (FIR) method, researchers have developed the application of rare earth-doped FE as optical $T$ sensor [20, 21]. Sui *et al.*[20] ever theoretically evaluated FL cooling involving $^4S_{3/2}$ and $^2H_{11/2}$ levels in 53$ZrF_4$-20$BaF_2$-3$LaF_3$-3$AlF_3$-20NaF-1$ErF_3$ (ZBLAN: $Er^{3+}$) glass with *in situ* optical $T$ sensing. To date, bicaloric $Er^{3+}$-doped FE with *in situ* optical $T$ sensing are yet to be developed.

One current area of focus in developing high value applications (such as solid-state refrigeration and sensors) for FE is to explore an efficient control technology for target-$T$ in portable devices and wearable electronics. Previously, $Sr_{0.7}Bi_{0.18}Er_{0.02}\square_{0.1}TiO_3$ (SBET, where □ represents strontium vacancies) heavily doped $Bi_{0.5}Na_{0.5}TiO_3$-0.06$BaTiO_3$ (BNT-0.06BT) FE exhibited a nearly hysteresis–free strain of ~0.11% and a maximum sensitivity of ~0.0032 $K^{-1}$ at 434 K[22]. In this letter, therefore, BNT-0.06BT-0.055SBET RFE is to investigate under multiple stimuli, i.e. *in situ* $E$, $T$ and photons, as well as to advance understanding of inherit microscopic phase structure/evolution during the dynamic process.

The ceramics of BNT-0.06BT-0.055SBET were prepared by a conventional solid-state reaction, as reported elsewhere[22]. Prior to perform electrical measurements, polished sample disks with a thickness of ~300 μm were coated with silver paste on one surface and then fired in air ambient batch-type furnace at 600 °C for 10 mins to produce test electrodes. Transparent indium tin oxides (ITO) film of ~200 nm in thickness was deposited on the other

surface by radio frequency magnetron sputtering with ITO target (99.99 %), which served as a top electrode for *in situ E*-Raman and FL measurements. Sputtering was performed under Ar gas pressure of 0.3 Pa with a flow of 30 SCCM and a power of 150 W. To ensure the uniformity of ITO films, the substrate holder was rotated at an autorotation speed of 20 rpm.

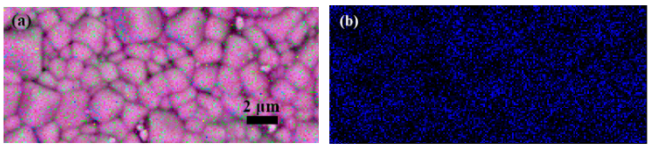


Fig. 1. SEM and EDS elemental mapping images of the BNT-0.06BT-0.055SBET ceramics.

Surface morphology was examined using scanning electron microscopy (SEM, Phenom ProX, Phenom-World BV, Netherlands). *E* induced polarization (*P*-*E*) and strain (*S*-*E*) were measured using a TF analyzer 2000E (aixACCT Systems GmbH, Aachen, Germany) at various *T*. FE test of electrodes was conducted in a silicon oil bath under an *E* in the form of triangular wave of 1 Hz. Direct EC effect was measured using a modified DSC (Q2000, TA Instruments, New Castle, DE) coupled with a ET2671A high-voltage source. Permittivity ($\varepsilon$) and loss tangent (tan $\delta$) of the samples were determined using an LCR meter (Agilent 4980A, Palo Alto, CA) at frequencies from 1 kHz to 1 MHz in a *T* range of 20-450 °C. *T* and *E* dependent UC spectra were obtained using a PL3-211-P spectrometer (HORIBA Jobin Yvon, France) with an external power-controllable 980 nm semiconductor laser (HJZ980-100, Hi-Tech Opto-electronics Company, Beijing, China) as the excitation source.

As shown in Fig. 1, the elemental mapping shows that Er is evenly distributed on the ceramic's surface, suggesting that $Er^{3+}$ ions have diffused into the host. We evaluate the electro-mechanical responses for the synthesized BNT-0.06BT-0.055SBET ceramics. As shown in Fig. 2a, the sprout-shape *S*-*E* curve presents a maximum strain of ~0.3%, together with two polarization current density *J*(*E*) peaks which at $E_B$ (backward sweeping) during electric unloading, revealing a typical characteristic of polymorphic phase transition[23, 24]. The mechanism responsible for such large strain has been previously hypothesized with a R matrix containing a residual FE phase and uncorrelated PNRs, as illustrated in the inset of Fig. 2a[25, 26]. A similar hypothetic system can be traced in our samples by a strong frequency dispersion feature in the $\varepsilon(T)$ response, as shown in Fig. 2b. Under a low *E* of less than 15 kV/cm, FE phase in R matrix produces low *P* and nearly zero strain in the *P*-*E* and *S*-*E* curves. When *E* reaches higher than 15 kV/cm, PNRs within R matrix nucleate and the isolated PNRs cluster, resulting in a gradual increase of strain. Upon the application of $E_F$≈30 kV/cm (forward sweeping), FE phase serves as a seed to induce the transformation from PNRs into long-range FE order, leading to a large total strain ($S_t$)[27].

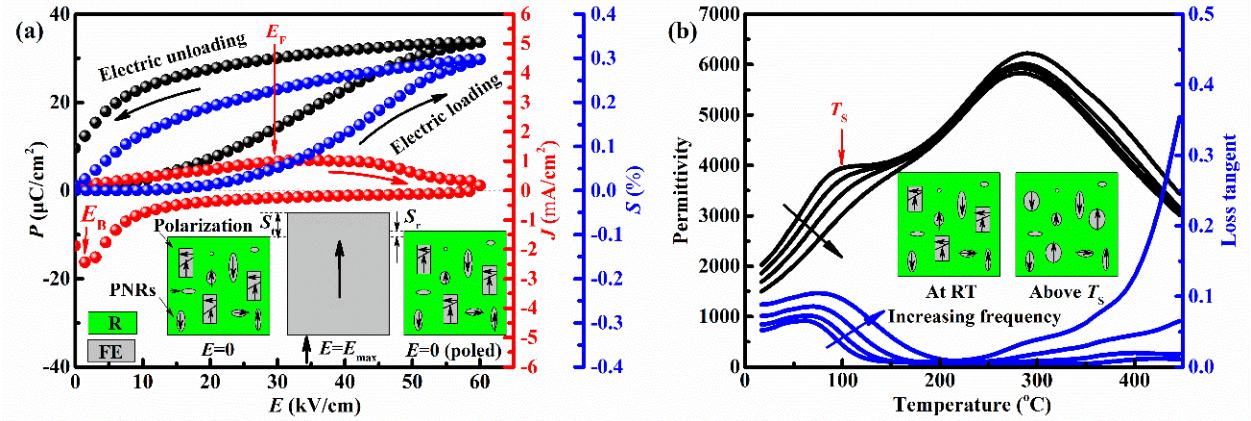


Fig. 2. (a) Unipolar *P*-*E*, *J*-*E*, *S*-*E* loops for the BNT-0.06BT-0.055SBET ceramics, and (b) *T* dependent $\varepsilon$ and tan$\delta$ for the poled BNT-0.06BT-0.055SBET ceramics. Insets show a model to explain its large *E* induced strain and thermal evolution of its microstructure, in which FE is ferroelectric phase, R is relaxor phase, $S_t$ is total strain, and $S_r$ is remnant strain.

For the BNT-0.06BT-0.055SBET ceramics, no obvious change of DSC heat flow was detected under a process of applying and removal *E*≤20 kV/cm. As shown in Fig. 3a, exothermal and endothermal peaks are observable with the application ('ON') and withdrawal ('OFF') of *E*≥30 kV/cm, respectively. A contribution of Joule heating to heat flow can be neglected due to the steady baseline after switching field on or off[28]. It is noted that exothermal peaks with field is stronger than endothermal ones without field in this sample, suggesting the presence of negative EC response, which is usually observed in BNT-based systems[29, 30]. Released ($Q_{exo}$) and adsorbed ($Q_{endo}$) heat can be determined by integrating exothermal and endothermal peaks, respectively, the difference of which is denoted as $\Delta Q$ ($\Delta Q$=$Q_{exo}$−$Q_{endo}$). As shown in Fig. 3b, under *E*=30 kV/cm, $\Delta Q$ is larger than $Q_{endo}$ at 20 °C and decreases below $Q_{endo}$ with *T* increasing up to 30 °C and then shows no obvious change with *T*. Whereas under *E*=40 kV/cm, both $Q_{endo}$ and $\Delta Q$ show higher value, which are nearly invariable with *T*. Upon increasing *E* up to 50 kV/cm and *T* up to 70 °C, the sample is easily broken down.

Compared with the above directly thermal-derived method, the polarization-deduced EC response can be in the form of higher *E* and *T* since *P*(*E*) test is conducted in a silicon oil bath. *P*-*E* loops measured under *E*=60 kV/cm in the *T* range of 20-150 °C are shown in Fig. 3c. Based on Maxwell's relation, adiabatic $\Delta T$ can be determined by

$$\Delta T = -\int_{E_1}^{E_2} \frac{T}{C(E,T)\rho}\left(\frac{\partial P}{\partial T}\right)_E dE, \qquad (1)$$

where $\rho$ is the mass density and $C(E, T)$ the heat capacity. Generally, $\left(\frac{\partial P}{\partial T}\right)_E$ derives from poly4 fittings of maximum polarization ($P_m$)-*T* curves at different maximum *E*, which is used

to calculate $\Delta T_m$, as shown in Fig. 3e. It is found that there exists negative EC response at $T \leq 80$ °C, which is different with positive EC response derived from the above direct measurement since the direct measurement with quasi-equilibrium process is different with the indirect one using non-equilibrium $P_m$. Domain switching usually involves instantaneous switching and switching with relaxation, leading to $P_m$ and remnant polarization ($P_r$) in $P(E)$ curves, respectively, which could contribute to equilibrium components of polarization. So, equilibrium components of polarization in isothermal $P$-$T$ curves can be approximated as a corrected polarization $P_{corr}=(P_m+P_r)/2$ [30]. As shown in Fig. 3d, the change of $P_{corr}$ with $T$ is small under $E \leq 20$ kV/cm, due to no obvious $J(E)$ peaks at $E_B$ (not shown here). Based on the above analysis, $\left(\frac{\partial P_{corr}}{\partial T}\right)_E$ instead of $\left(\frac{\partial P_m}{\partial T}\right)_E$ is used to calculate EC effect and $\Delta T_{corr}$ at various $T$ is plotted in Fig. 3e. It is found that there still exists negative EC response under $E \leq 30$ kV/cm at 20 °C, as a result of the increase in dipolar disorder caused by $E$ driven nucleation and clustering of PNRs. Whereas under $E \geq 40$ kV/cm at 20 °C, positive EC response is observable and $\Delta T_{corr}$ increases up to 0.7 K with increasing $E$ up to 60 kV/cm, due to $E$ induced transformation from PNRs into long-range FE order. Interestingly, $\Delta T_{corr}$ increases with increasing $T$ and reaches a maximum (3.3 K) at $T_S \approx 100$ °C under $E \geq 40$ kV/cm, which is likely to a thermal evolution from residual FE phase to PNRs[31].

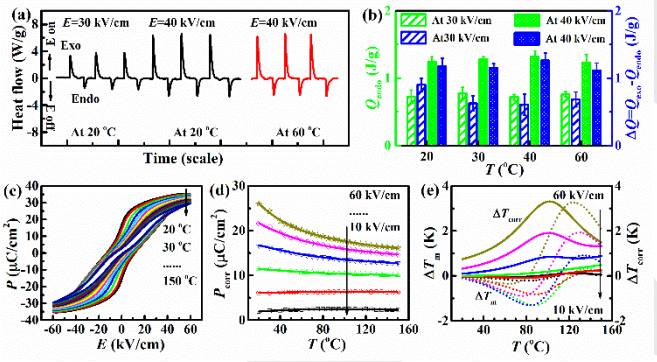


Fig. 3 (a) DSC heat flow measured at various $T$ under a process of applying and removal $E$=30 and 40 kV/cm for the BNT-0.06BT-0.055SBET ceramics, (b) the relation between $Q_{endo}$, $\Delta Q(=Q_{exo}-Q_{endo})$ and $T$ under $E$=30 and 40 kV/cm, (c) $T$ dependent $P$-$E$ loops measured under $E$=60 kV/cm, (d) $T$ dependent $P_{corr}(=(P_m+P_r)/2)$ under various $E$, and (e) $\Delta T_m$ and $\Delta T_{corr}$ at various $E$ and $T$.

UC emission spectra ($\lambda_{ex}$=980 nm) of the material in the $T$ range of 20–280 °C are displayed in Fig. 4a, including two parts: two strong $^2H_{11/2}/^4S_{3/2} \rightarrow ^4I_{15/2}$ green emission transitions at ~531 nm and ~552 nm, respectively, and a weak $^4F_{9/2} \rightarrow ^4I_{15/2}$ red emission transition at ~663nm. All emission bands correspond to the results reported for other ceramics [32, 33] and nanocrystals [34] doped with $Er^{3+}$. As shown in Fig. 4b, $T$-dependent $^2H_{11/2}/^4S_{3/2} \rightarrow ^4I_{15/2}$ FL intensities (denoted as $I_H$ and $I_S$, respectively) were normalized to the integral at 20 °C. It is clear that $I_H$ increases steadily with the increase of $T$ from 20 to 100 °C and then decreases as $T$ is further increased, while $I_S$ persistently decreases. Noticeably, the sum of $I_H$ and $I_S$ decreases with $T$, as a result of thermal quenching[35]. The maximized $I_H$ occurs at $T_S \sim 100$ °C, which is due to the population inversion from the $^4S_{3/2}$ to $^2H_{11/2}$ levels, as shown in Fig. 4c. Herein, an incoherent regime consisting of both FE phase and PNRs below $T_S \sim 100$ °C (the inset of Fig. 2b), where the dephasing time is shorter than the laser pulse duration, support population inversion through $^4S_{3/2} \rightarrow ^2H_{11/2}$ transition[36, 37]. This implies that "self-cooling" effect is referred as removal of excess heating due to non-radiative recombination, which can sustain high $T$ operation of ~100 °C.

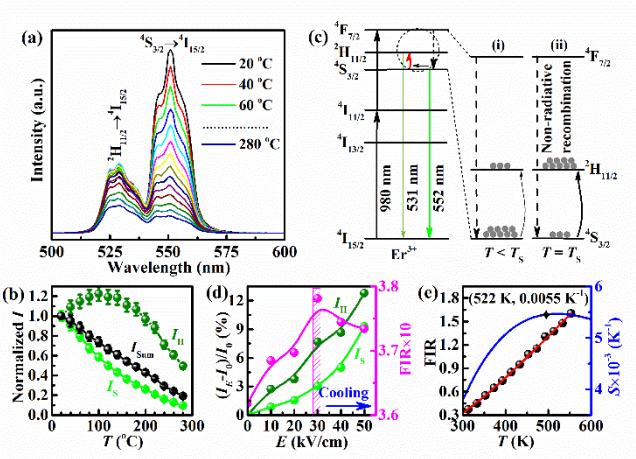


Fig. 4 (a) UC emission spectra ($\lambda_{ex}$=980 nm) measured at various $T$ for the BNT-0.06BT-0.055SBET ceramics, (b) $T$ dependent normalized FL intensities, (c) simplified model of the phase-transition-induced population inversion process at (i) $T<T_S$ and (ii) $T=T_S$ between $^2H_{11/2}$ and $^4S_{3/2}$ levels, (d) $E$ dependent $(I_E-I_0)/I_0$ for $^2H_{11/2}/^4S_{3/2} \rightarrow ^4I_{15/2}$ transitions and FIR, (e) $T$ dependent FIR and sensitivity *vs.* $T$

Since the amount of self-cooling is related to FIR ($I_H/I_S$ ratio), an *in-situ* $E$ was applied to modulate its FIR. Applying $E$ can slightly enhance its UC emission intensity (not shown here). It is clear from Fig. 4d that the increases in $I_H$ and $I_S$ are almost linear under $E \leq 30$ kV/cm, as a result of the breaking of local crystal field symmetry of $Er^{3+}$ luminescent center derived from atomic interaction along polar axis[38] and the nucleation and clustering of PNRs within R matrix. A further increase in $E$ induces a transition from PNRs into long-range FE order, leading to a remarkable increase up to ~12% and ~10% at $E$=50 kV/cm for $I_H$ and $I_S$, respectively. As a result, $I_H/I_S$ gradually increases with increasing $E$ and then reach its saturation value at $E$=30 kV/cm. $E \geq 30$ kV/cm induced cooling can be detected by the reduction in $I_H/I_S$. The further study is need to quantize the amount of FL cooling.

FIR increases monotonously with $T$, as shown in Fig. 4e, which fits well in the expression of $FIR=A\exp(-\Delta E_{HS}/k_B T)$, where $A$, $\Delta E_{HS}$ and $k_B$ are auxiliary constant, representing the energy gap between $^2H_{11/2}$ and $^4S_{3/2}$ levels and Boltzmann constant, respectively. Furthermore, optical thermal sensitivity calculated using the formula $S(T)=d(FIR)/dT$ increases with $T$ and reaches a maximum value of 0.0055 $K^{-1}$ at 522 K, as plotted in the inset of Fig. 4e. For comparison, the sensitivity value of this material is greater than those of ZBLAN:$Er^{3+}$ glass[20], $NaLuF_4$:$Er^{3+}$/$Yb^{3+}$ microcrystals [21] and other $Er^{3+}$-doped FE ceramics [33, 39-41], and is comparable to those of $LiNbO_3$:$Er^{3+}$/$Yb^{3+}$ particles [42] and $BaTiO_3$:$Er^{3+}$ nanocrystals [43]. It was reported that higher thermal sensing was found in rare-earth doped nanoscale hosts [44] and also higher efficient UC luminescence was achieved through 1530 nm excitation [34]. EC and FL cooling of Er-doped nanoscale FE host is need to further study.

In conclusion, a new ternary solid solution of BNT-0.06BT-0.055SBET was prepared using a conventional solid-state reaction

method. R matrix that contained FE phase and PNRs produced a large positive EC response of $\Delta T_{corr}$=0.7 K under $E$=60 kV/cm at RT, a FL cooling and a maximum $T$ sensitivity of 0.0055 $K^{-1}$ at 522 K. Interestingly, both $\Delta T_{corr}$ and $I_H$ increase with increasing $T$ and reaches a maximum at $T_S$≈100 °C. More, an *in-situ E* can modulate the amount of cooling by tuning the $I_H/I_S$ ratio in the novel material, i.e., the amount of cooling is more effective above 30 kV/cm than that at 30 kV/cm due to the reduction in $I_H/I_S$. The increase in the $I_H/I_S$ ratio was attributed to a phase-transition-induced population inversion from the $^4S_{3/2}$ to $^2H_{11/2}$ state. The proposed novel luminescent FE exhibits a large positive EC response and better $E$ - and $T$-dependent luminescent properties with *in situ* optical $T$ sensing, which make this material promising candidates for all-solid-state cryocoolers for portable devices and wearable electronics in the future.

**Funding.** Natural Science Foundation of Zhejiang Province (LY16E020005)

**Acknowledgment**. We thanks Prof. Yifeng Hu and Prof. Hua Zou for the preparation of Transparent ITO electrode, Prof. Wangfeng Bai, Prof. Peng Zheng and Prof. Fei Wen for discussion about microstructural mechanism, and Prof. Xihong Hao and Dr. Ye Zhao for DSC measurement.

**Disclosures**. The authors declare no conflicts of interest.

## References

1. T. Gottschall, D. Benke, M. Fries, A. Taubel, I.A. Radulov, K.P. Skokov, and O. Gutfleisch, Adv. Funct. Mater. **27**, 1606735 (2017).
2. J. He and T.M. Tritt, Science **357**, 1 (2017).
3. Y. Taguchi, H. Sakai, and D. Choudhury, Adv. Mater. **29**, 1606144 (2017).
4. B. Li, Y. Kawakita, S. Ohira-Kawamura, T. Sugahara, H. Wang, J. Wang, Y. Chen, S.I. Kawaguchi, S. Kawaguchi, K. Ohara, K. Li, D. Yu, R. Mole, T. Hattori, T. Kikuchi, S.I. Yano, Z. Zhang, Z. Zhang, W. Ren, S. Lin, O. Sakata, K. Nakajima, and Z. Zhang, Nature **567**, 506 (2019).
5. J. Tušek, K. Engelbrecht, D. Eriksen, S. Dall'Olio, J. Tušek, and N. Pryds, Nat. Energy **1**, 1 (2016).
6. R. Ma, Z. Zhang, K. Tong, D. Huber, R. Kornbluh, Y.S. Ju, and Q. Pei, Science **357**, 1130 (2017).
7. Q. Zhang, X. Liu, M.I. Utama, G. Xing, T.C. Sum, and Q. Xiong, Adv. Mater. **28**, 276 (2016).
8. B. Peng, Q. Zhang, B. Gang, G.J.T. Leighton, C. Shaw, S.J. Milne, B. Zou, W. Sun, H. Huang, and Z. Wang, Energy & Environmental Science **12**, 1708 (2019).
9. X.S. Wang, C.N. Xu, H. Yamada, K. Nishikubo, and X.G. Zheng, Adv. Mater. **17**, 1254 (2005).
10. R. López-Juárez, R. Castañeda-Guzmán, F. Rubio-Marcos, M.E. Villafuerte-Castrejón, E. Barrera-Calva, and F. González, Dalton T. **42**, 6879 (2013).
11. K. Li, L. Luo, Y. Zhang, W. Li, and Y. Hou, ACS Appl. Mater. Inter. **10**, 41525 (2018).
12. J.C. Zhang, C. Pan, Y.F. Zhu, L.Z. Zhao, H.W. He, X. Liu, and J. Qiu, Adv. Mater. **30**, e1804644 (2018).
13. Q.M. Zhang and T. Zhang, Science **357**, 1094 (2017).
14. E. Defay, R. Faye, G. Despesse, H. Strozyk, D. Sette, S. Crossley, X. Moya, and N.D. Mathur, Nat. Commun. **9**, 1827 (2018).
15. X.D. Jian, B. Lu, D.D. Li, Y.B. Yao, T. Tao, B. Liang, J.H. Guo, Y.J. Zeng, J.L. Chen, and S.G. Lu, ACS Appl. Mater. Inter. **10**, 4801 (2018).
16. B.Z. Shen, Y. Li, and X. Hao, ACS Appl. Mater. Inter. **11**, 34117 (2019).
17. M. Sheik-Bahae and R.I. Epstein, Nat. Photonics **1**, 693 (2007).
18. M.P. Hehlen, M. Sheik-Bahae, R.I. Epstein, S.D. Melgaard, and D.V. Seletskiy, J. Mater. Chem. C **1**, 7471 (2013).
19. R.I. Epstein, M.I. Buchwald, B.C. Edwards, T.R. Gosnell, and C.E. Mungan, Nature **377**, 500 (1995).
20. G. Sui, X. Li, L. Cheng, J. Sun, J. Zhang, X. Zhang, H. Xia, R. Hua, and B. Chen, Sensor. Actuat. B **220**, 362 (2015).
21. Q. Qiang, S. Du, X. Ma, W. Chen, G. Zhang, and Y. Wang, Dalton T. **47**, 8656 (2018).
22. H. Pan, J. Zhang, X. Jia, H. Xing, J. He, J. Wang, and F. Wen, Ceram.Int. **44**, 5785 (2018).
23. H.S. Han, W. Jo, J. Rodel, I.K. Hong, W.P. Tai, and J.S. Lee, J. Phys. Conden. Matter. **24**, 365901 (2012).
24. J. Wu, D. Xiao, and J. Zhu, Chem. Rev. **115**, 2559 (2015).
25. D. Gobeljic, R. Dittmer, J. Rödel, V.V. Shvartsman, D.C. Lupascu, and S. Zhang, J. Am. Ceram. Soc. **97**, 3904 (2014).
26. T.H. Dinh, J.-K. Kang, J.-S. Lee, N.H. Khansur, J. Daniels, H.-Y. Lee, F.-Z. Yao, K. Wang, J.-F. Li, H.-S. Han, and W. Jo, J. Eur. Ceram. Soc. **36**, 3401 (2016).
27. T. Li, X. Lou, X. Ke, S. Cheng, S. Mi, X. Wang, J. Shi, X. Liu, G. Dong, H. Fan, Y. Wang, and X. Tan, Acta Mater. **128**, 337 (2017).
28. M. Sanlialp, V.V. Shvartsman, M. Acosta, B. Dkhil, and D.C. Lupascu, Appl. Phys. Lett. **106**, 062901 (2015).
29. F. Li, G. Chen, X. Liu, J. Zhai, B. Shen, H. Zeng, S. Li, P. Li, K. Yang, and H. Yan, J. Eur. Ceram. Soc. **37**, 4732 (2017).
30. Z. Jiang, G.-P. Zheng, and S. Ullah, Ceram. Int. **45**, 2876 (2019).
31. G. Viola, H. Ning, X. Wei, M. Deluca, A. Adomkevicius, J. Khaliq, M. John Reece, and H. Yan, J. Appl. Phys. **114**, 014107 (2013).
32. W. Li, Z. Xu, R. Chu, P. Fu, and G. Zang, J. Alloys Compd. **583**, 305 (2014).
33. X. Jia, J. Zhang, Y. Gao, J. Wang, and P. Zheng, Mater. Res. Bull. **89**, 11 (2017).
34. L. Liu, K. Lu, L. Xu, D. Tang, C. Liu, M.K. Shahzad, D. Yan, F. Khan, E. Zhao, and H. Li, Opt. Lett. **44**, 711 (2019).
35. Q. Zhang, K. Chen, L. Wang, H. Sun, X. Wang, and X. Hao, J. Mater. Chem. C **3**, 5275 (2015).
36. J.H. Quilter, A.J. Brash, F. Liu, M. Glassl, A.M. Barth, V.M. Axt, A.J. Ramsay, M.S. Skolnick, and A.M. Fox, Phys. Rev. Lett. **114**, 137401 (2015).
37. X. Xu, W. Zhang, D. Yang, W. Lu, J. Qiu, and S.F. Yu, Adv. Mater. **28**, 8045 (2016).
38. M. Acosta, L.A. Schmitt, L. Molina-Luna, M.C. Scherrer, M. Brilz, K.G. Webber, M. Deluca, H.J. Kleebe, J. Rodel, and W. Donner, J. Am. Ceram. Soc. **98**, 3405 (2015).
39. A.S.S. de Camargo, J.F. Possatto, L.A.d.O. Nunes, É.R. Botero, É.R.M. Andreeta, D. Garcia, and J.A. Eiras, Solid State Commun. **137**, 1 (2006).
40. X. Chai, J. Li, X. Wang, H. Zhao, Y. Li, and X. Yao, Materials Sci. Eng. B **201**, 23 (2015).
41. P. Du, L. Luo, W. Li, and Q. Yue, J. Appl. Phys. **116**, 014102 (2014).
42. M. Quintanilla, E. Cantelar, F. Cussó, M. Villegas, and A.C. Caballero, Appl. Phys. Express **4**, 022601 (2011).
43. M.A.R.C. Alencar, G.S. Maciel, C.B. de Araújo, and A. Patra, Appl. Phys. Lett. **84**, 4753 (2004).
44. E.C. Ximendes, U. Rocha, K.U. Kumar, C. Jacinto, and D. Jaque, Appl. Phys. Lett. **108**, 253103 (2016).